Publication I

Ranran Lin, Ari Haavisto, and Antero Arkkio. 2009. Validation of a time-harmonic numerical model for solving magnetic field in end region of a radial-flux machine. IEEE Transactions on Magnetics, volume 45, number 12, pages 5360-5367.

Validation of a Time-Harmonic Numerical Model for Solving Magnetic Field in End Region of a Radial-Flux Machine

Ranran Lin, Ari Haavisto, and Antero Arkkio

Department of Electrical Engineering, Faculty of Electronics, Communications and Automation, Helsinki University of Technology, Espoo, Finland

We present an analysis of the magnetic field in the end region of a radial-flux rotating machine. In numerical simulations, we used three familiar boundary conditions to replace the modeling of the end shields and frame. We made measurements for comparison, and the simulation results were quite consistent with the measurements. Our analysis shows that the eddy current in the end shields and frame influences the magnetic field in the end region slightly and that the use of a homogeneous Neumann boundary condition or a standard impedance boundary condition (SIBC) to replace the end shields and frame can solve the magnetic field in the end region more accurately than a homogeneous Dirichlet boundary condition. Validation by the measurements demonstrates that 3-D current-driven time-harmonic model with suitable boundary conditions can be used to solve the magnetic field in the end region quite accurately.

Index Terms—**Boundary condition, end-winding, finite element analysis, magnetic flux, measurement.**

I. Introduction

In A radial-flux rotating electric machine, the current flowing through the end-winding produces magnetic flux, which is referred to as end-winding leakage. In general, the end-winding leakage originates from both a stator end-winding and the end structures of a rotor, e.g., the end-ring of a squirrel-cage rotor. However, what is usually searched for is the stator end-winding leakage because many electromagnetic phenomena in the end region relate to it, e.g., eddy current [1]–[4], magnetic forces and stresses [5]–[9], mechanical vibrations [10], [11], and temperature-rise and cooling [12]–[14]. Moreover, some parameters relating to the stator end-winding leakage are required, e.g., end-winding leakage reactance for calculating the starting current and starting torque [15]–[18]. Whichever aspect mentioned above needs studying, the analysis of the magnetic field is a starting point.

In the active region of an electric machine, magnetic induction vectors rotate in a plane of the electrical steel laminations, namely, 2-D rotating magnetic flux [19]. However, in the end region, the rotating magnetic flux is always three-dimensional.

In the past decades, some studies relating to the magnetic field in the end region were done by both analytical and numerical methods. Recently, the finite-element method (FEM) has been increasingly used because it can tackle complicated structures with reasonable assumptions and reliable results.

In most analytical studies, the coil ends were modeled as infinitely thin conductors and no eddy current was taken into account in the end region. Many analytical studies, by using Biot-Savart's law, dealt with the end-winding reactance [16], [17], [20], and the magnetic forces on the end-winding [21], etc.

Several numerical studies, based on finite-element analyses (FEAs) [22], [23], were concentrated on solving the magnetostatic field in the end region. Because the eddy current was not considered in these studies, the mesh in the FEAs did not need to be very dense, and the computation was relatively fast. However, the eddy current in the end region may, to some extent, affect the distribution of the magnetic field.

Moreover, some numerical studies used axisymmetric models and took a part of the eddy current into account, for example, the eddy current in the finger plates, clamping plates, or end shields, etc., [14], [24]–[26]. They provide more accurate results than the magnetostatic models. Nevertheless, the axisymmetric end region is still a rough simplification because the stator end-winding is absolutely three-dimensional.

Recently, 3-D numerical simulations have been increasingly applied to the analysis of the end region [3], [6], [15], [27]–[29]. Under the circumstances, the stator end-winding could be modeled accurately. However, a problem of modeling the frame and end shields arose. Owing to the high isotropic conductivity and permeability, the skin depth was normally less than 1 mm, so the finite elements there should be quite small to model the eddy current accurately. Nonetheless, in 3-D simulations of large machines, such a dense mesh would cause such a large number of degrees of freedom (DOFs) that a computer was not capable of solving them. Consequently, few studies include these parts during the course of the modeling. Actually, one possible way to model the eddy current there is to use a standard impedance boundary condition (SIBC) under time-harmonic simulations. However, none of studies has applied the SIBC to the analysis of the end region yet.

In this paper, the model of the stator end-winding was created according to its measured geometric coordinates. Numerical simulations were carried out based on 3-D time-harmonic FEAs by a commercial software package, and the end shields and frame were modeled by three different boundary conditions. Finally, practical measurement was done on the same machine to validate the simulation results.

II. Description of Test Machine

To study the end-winding leakage quantitatively, a reliable way is to calculate the magnetic flux passing through a closed loop along a coil end, instead of just measuring the magnetic induction in the end region.

Manuscript received December 18, 2008; revised April 10, 2009. Current version published November 18, 2009. Corresponding author: R. Lin (e-mail: ranran.lin@gmail.com).

Color versions of one or more of the figures in this paper are available online at http://ieeexplore.ieee.org.

Digital Object Identifier 10.1109/TMAG.2009.2022934

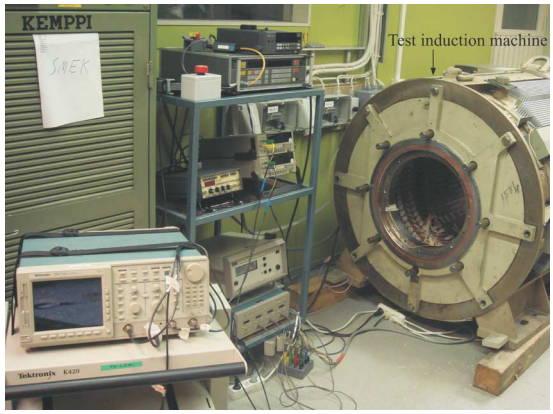

Fig. 1. Stator of the induction machine and some measurement devices.

TABLE I
MAIN SPECIFICATIONS OF TEST MACHINE

Parameter	Value
Rated power (MW)	2.24
Rated frequency (Hz)	50
Axial length of stator core (mm)	1000
Outer diameter of stator core (mm)	980
Inner diameter of stator core (mm)	670
Number of pole pairs	2
Number of stator slots	72
Number of parallel branches	4
Number of turns in series in a stator coil	3
Coil span of a stator coil (stator slot pitches)	16
Connection of stator windings	Star

For the purpose of testing, a machine with a well-defined form-wound winding, e.g., a diamond winding, is better than that with a random-wound winding, for the current in the form-wound winding can be accurately determined. Usually, a diamond winding is installed in machines with a power range of more than 1 MW [30]. Therefore, a 3-phase, 4-pole, 2.24-MW squirrel-cage induction machine with a two-layer diamond winding was used as a test machine. Because it was impossible to test the machine at full load in the laboratory, the rotor was taken away and the stator thus was able to be tested at rated current. The machine is shown in Fig. 1 and its main specifications are listed in Table I.

III. NUMERICAL SIMULATIONS

A. 3-D Numerical Model

In the numerical model, the coil ends in the diamond winding were created by measuring the 3-D coordinates of the nose, involute, and knuckle parts, as shown in Fig. 2. The rest were created according to the specifications of the machine.

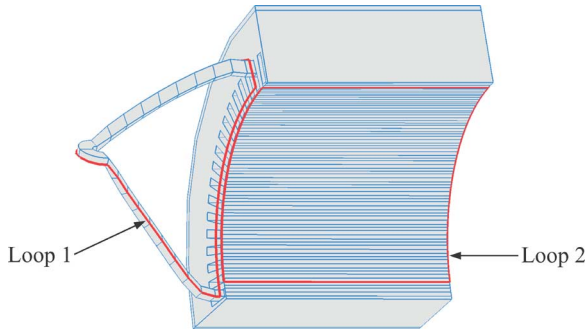

Fig. 2. Model of a coil end as well as the models of two loops.

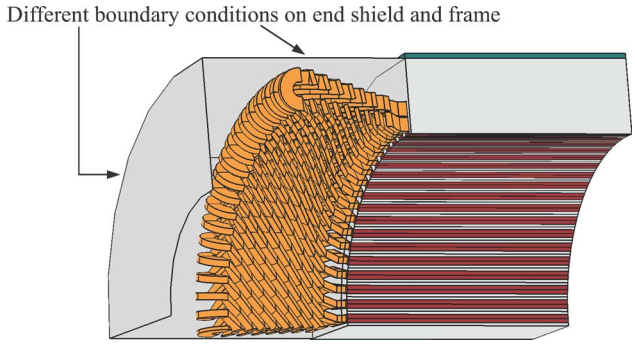

Fig. 3. The 3-D numerical model (without the air region) and the surfaces to which different boundary conditions were applied.

Thanks to the symmetry and periodicity, the axial length of the model was half of the full length, and the cross-section perpendicular to the axial direction was a pole pitch sector.

The skin depth of the end shields and frame was only 1 mm at rated frequency. To reflect the change of the eddy current in this 1-mm-thick region, the maximum size of the elements should be limited to less than 0.5 mm, otherwise the modeling of the eddy current would not be accurate. Because only tetrahedral elements were allowed to be used in this region, around 1.3×10^6 DOFs would be generated, and it was impossible to solve them by the computer because of the limit of the computer memory. Therefore, three familiar boundary conditions were used to model these parts, and a part of the frame attaching the stator core was also included in the model. Fig. 3 shows the geometry of the model.

The stator core was anisotropic in both reluctivity and conductivity, and the rest of the materials were isotropic. The relative permeability tensor of the core was $1000\boldsymbol{e}_x\boldsymbol{e}_x + 1000\boldsymbol{e}_y\boldsymbol{e}_y + 50\boldsymbol{e}_z\boldsymbol{e}_z$, where $\boldsymbol{e}_x\boldsymbol{e}_x$, $\boldsymbol{e}_y\boldsymbol{e}_y$, and $\boldsymbol{e}_z\boldsymbol{e}_z$ are the unit dyads in the $x-y-z$ Cartesian coordinate system. The relative permeability of the slot wedges was 4.7.

Two infinitely thin loops were created so as to calculate the magnetic flux passing through them, as shown in Fig. 2. Loop 1 in the end region was along a coil end, and loop 2 in the active region was attached to the surface of the stator core. The circumferential length of loop 2 was one coil pitch, so these two loops, actually, matched half of one stator coil.

B. Simulations by Time-Harmonic FEA

In the time-harmonic FEA, the stator winding was current-driven, and the current value was $N\tilde{I}_{\rm ph}^{\rm str}/a$, where $\tilde{I}_{\rm ph}^{\rm str}$ is the rms value of stator phase current; N is the number of turns in series in a stator coil; and a is the number of parallel branches. In this machine, $N=3$, $a=4$, and $\tilde{I}_{\rm ph}^{\rm str}$ was set at 500 A, 832 A, and 1000 A, respectively, corresponding to underload, full load, and overload, respectively.

The governing equation was

$$\nabla\times[\boldsymbol{\nu}\cdot(\nabla\times\underline{\boldsymbol{A}})]+\mathrm{j}\omega\boldsymbol{\sigma}\cdot\underline{\boldsymbol{A}}-\underline{\boldsymbol{J}}_{\rm s}=\boldsymbol{0} \tag{1}$$

where ∇ is the vector differential operator; $\underline{\boldsymbol{A}}$ and $\underline{\boldsymbol{J}}_{\rm s}$ are complex vectors of magnetic vector potential and source current density, respectively; $\boldsymbol{\nu}$ and $\boldsymbol{\sigma}$ are reluctivity and conductivity tensors, respectively; ω is an angular frequency; and j is the imaginary unit. The eddy-current density $\mathrm{j}\omega\boldsymbol{\sigma}\cdot\underline{\boldsymbol{A}}$ is considered in the conducting parts except the stator winding. Only $\underline{\boldsymbol{J}}_{\rm s}$ was considered in the stator winding.

Galerkin's method was used in the weak form of method of weighted residual for the finite element discretization. Two types of first-order edge-based elements, i.e. tetrahedra and prisms, were used in the end region and active region, respectively. The number of DOFs was 672 370.

C. Assignment of Boundary Conditions

In the $r-\varphi-z$ cylindrical coordinate system, such a periodic condition was imposed that the components of the magnetic vector potential on the two sides, that is, $\underline{A}_r^{\rm I}$, $\underline{A}_\varphi^{\rm I}$, and $\underline{A}_z^{\rm I}$ on one side, and $\underline{A}_r^{\rm II}$, $\underline{A}_\varphi^{\rm II}$, and $\underline{A}_z^{\rm II}$ on the other side, satisfied the condition $\underline{A}_r^{\rm I}=(-1)^i\underline{A}_r^{\rm II}$, $\underline{A}_\varphi^{\rm I}=(-1)^i\underline{A}_\varphi^{\rm II}$, and $\underline{A}_z^{\rm I}=(-1)^i\underline{A}_z^{\rm II}$, where i is the number of poles to be modeled.

The 3-D simulations were done under three cases, corresponding to three boundary conditions used to model the end shield and frame as pointed out in Fig. 3.

1) Case 1: A homogeneous Dirichlet boundary condition was imposed as

$$\underline{\boldsymbol{A}}\times\boldsymbol{n}=\boldsymbol{0} \tag{2}$$

where $\boldsymbol{n}$ is an outward-directed normal unit vector.

2) Case 2: A homogeneous Neumann boundary condition was imposed as

$$\nabla\times\underline{\boldsymbol{A}}\times\boldsymbol{n}=\boldsymbol{0}. \tag{3}$$

3) Case 3: An SIBC was imposed as

$$\boldsymbol{n}\times\underline{\boldsymbol{E}}=Z_{\rm s}\boldsymbol{n}\times(\boldsymbol{n}\times\underline{\boldsymbol{H}}) \tag{4}$$

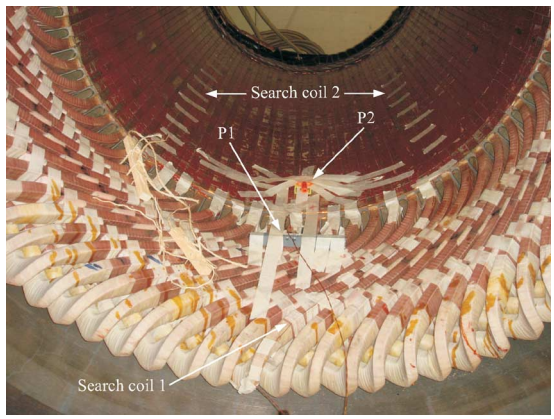

Fig. 4. Two search coils fixed in the test machine and two measured points for magnetic induction.

where $\underline{\boldsymbol{E}}$ and $\underline{\boldsymbol{H}}$ are electric field strength and magnetic field strength, respectively; $Z_{\rm s}$ is the standard surface impedance, which was derived from

$$Z_{\rm s}=\sqrt{\frac{\pi f\mu}{\sigma}}(1+\mathrm{j}) \tag{5}$$

where f denotes a frequency; μ and σ denote permeability and conductivity, respectively. By using the SIBC, the eddy current in the end shield and frame was considered as surface current flowing along the boundary. The consideration was reasonable since the thickness of these parts was at least 10 mm and the skin depth was just 1 mm.

Besides, among the boundaries of the frame in the active region, the one which was perpendicular to the axial direction and connected the boundary with different conditions mentioned above, applied $\nabla\times\underline{\boldsymbol{A}}\times\boldsymbol{n}=\boldsymbol{0}$ in all the cases. On the other boundaries, $\underline{\boldsymbol{A}}\times\boldsymbol{n}=\boldsymbol{0}$ was used in all the cases.

IV. Practical Measurement

A. Construction of Search Coils

To calculate the magnetic flux, two one-turn search coils, which were made of enamelled copper wires whose diameter was 0.5 mm, were fixed in the test machine. They were similar to the loops in the numerical model, as shown in Fig. 4.

As for search coil 1 in the end region, the enamelled wire was fixed on the surface of a coil end. Insulating tapes were used to fix the wire on the upper part of the coil end, and plastic cords were used to fix the wire on the lower part. The connection wires were intertwined so that no magnetic flux could pass through them.

Search coil 2 was made similarly. The enamelled wire was fixed on the surface of the core by insulating tapes. The axial length of search coil 2 equalled the axial length of the core, and

accordingly the area encircled by it was twice as large as that encircled by loop 2 in the numerical model.

B. Primary Measurement

Each search coil was connected to a multimeter to measure the rms value of the induced electromotive force (EMF) in itself. Two current transformers (CTs) were used and the CTs were connected to a power analyzer to measure the rms value of the stator phase current.

Besides, the waveforms of the stator phase current, stator phase voltage, and induced EMF of the search coils were recorded by a 4-channel oscilloscope. Owing to the relatively high voltage of the stator winding, a 4-channel isolator was connected to the oscilloscope to avoid damaging it.

Magnetic induction at two points in the machine were measured by a Gauss/Tesla meter. The stator phase voltage was measured by a multimeter as well.

C. Secondary Measurement

The ventilator was not installed in the machine, so measuring the temperature in the winding was necessary. The temperature was obtained by a data acquisition unit, which was connected to six Pt100 temperature sensors. The measured temperature should not exceed 120 °C.

D. Process of Practical Measurement

The rated current of the test machine was 832 A, so the range of the stator phase current in the measurement was chosen between 0 A and 1000 A. Since the temperature in the winding and stator core rose rapidly as the current increased, the current at first rose to 1000 A, and then reduced to 0 A by a step of 50 A, so that the temperature nearly remained constant. There were 21 measured points in total, and the rms values of the induced EMFs were recorded at each point. Furthermore, when the current reached 500 A, 832 A, and 1000 A, respectively, corresponding waveforms were recorded, and magnetic induction at two points was also checked.

V. Results and Analysis

A. Degree of Nonlinearity of Magnetic Circuit

The degree of nonlinearity of the magnetic circuit in an electric machine determines analysis types. The magnetic circuit in a real electric machine is definitely nonlinear, by reason of the saturation of the core. However, if the nonlinearity is not serious in the region to be studied, linear time-harmonic analyses can be used, and they can save the computation time enormously with reliable results, in particular in complicated 3-D numerical simulations.

Fig. 5 plots the rms values of the EMFs induced in the search coils during the measurement. The curve relating to search coil 1 is a straight line, whereas the one relating to search coil 2 is not an exactly straight line. This phenomenon means that slight nonlinearity occurs in the magnetic circuit of the active region, and it probably results from the saturation of the magnetic slot wedges. Anyway, time-harmonic analyses can be used to analyze the whole model, for the nonlinearity in the active region is not so evident.

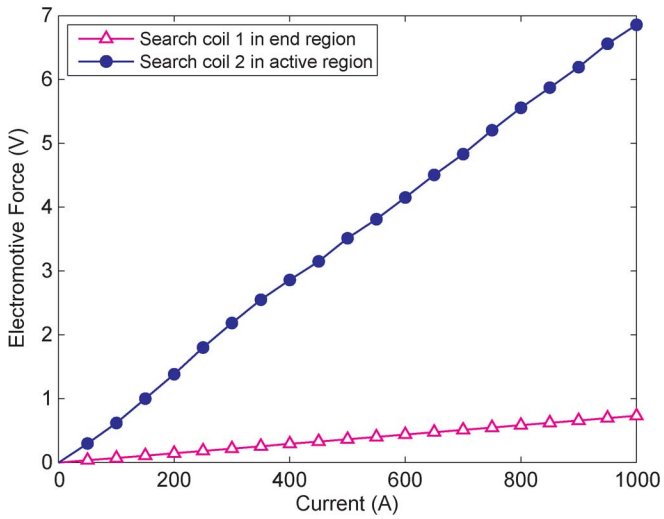

Fig. 5. Variations in the EMFs induced in the search coils as a function of the stator phase current.

B. Waveforms of Voltage, Current, and EMF

During the measurement, when the stator phase current reached 500 A, 832 A, and 1000 A, respectively, waveforms were recorded and illustrated in Fig. 6. Fig. 6(a) shows the waveforms of the stator voltage when the current reached 832 A. The waveforms of the voltage at the other current values are the same. It is clear that the waveforms of the stator phase current, illustrated in Fig. 6(b), are closer to a sinusoidal function than the waveforms of the stator voltage in Fig. 6(a).

In Fig. 6(c) and 6(d), the variations in the EMFs induced in the two search coils are not exactly sinusoidal functions of time, especially in Fig. 6(d). In other words, the sinusoidal stator current produced slightly nonsinusoidal magnetic flux. It is understandable that the nonsinusoidal waveforms in Fig. 6(d), corresponding to search coil 2, result from the nonlinearity of the saturated stator core, especially the magnetic slot wedges. It is also clear in Fig. 6(d) that the distortions become more distinct as the current increases. The nonsinusoidal waveforms in Fig. 6(c), relating to search coil 1, probably result from the eddy current flowing in the end shields and frame made of ferromagnetic materials. Because the eddy current pushes the magnetic flux towards the inner surface of the end shields and frame, it only flows in a thin layer close to the inner surface, and saturation appears in the thin layer. Even if the stator current is quite small, the eddy current is always induced in this part, and it, more or less, leads to saturation in the end region. In comparison with Fig. 6(d), the distortions of the waveforms in Fig. 6(c) are slight, and therefore the nonlinearity in the end region is not so distinct as in the active region.

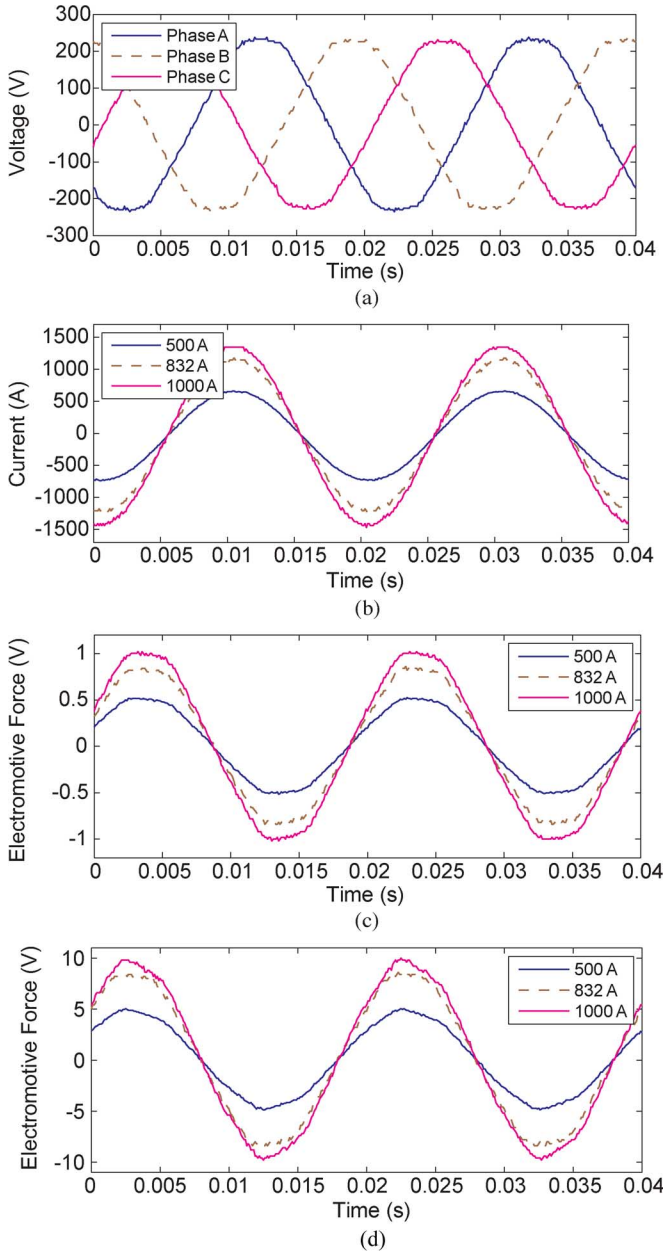

Fig. 6. Some recorded waveforms in the measurement: (a) the waveforms of the three-phase voltage at the current value 832 A; (b) the waveforms of the stator phase current; (c) the waveforms of the induced EMF in search coil 1 in the end region; and (d) the waveforms of the induced EMF in search coil 2 in the active region.

A discrete Fourier transform (DFT) with a frequency resolution of 6.25 Hz was performed on the EMF induced in search coil 1 at rated current as

$$X[k] = \sum_{n=0}^{M-1} \mathrm{e}^{-\mathrm{j}\frac{2\pi}{M}nk} x[n], \quad k = 0, 1, 2, \ldots, M-1 \tag{6}$$

where $x[n]$ denotes a finite-length sequence; M is the length of the sequence; and $X[k]$ represents the DFT of the sequence $x[n]$. To show the relative magnitude of each component, the common logarithm of the magnitude (unit in mV), $\lg(2|X[k]|/M)$, is plotted in Fig. 7. Apart from the fundamental frequency, there

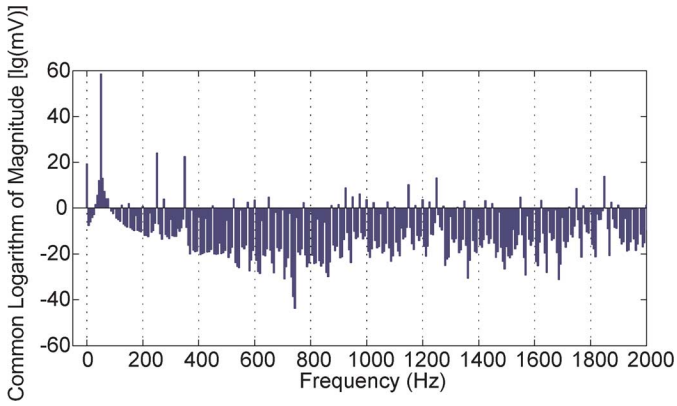

Fig. 7. Common logarithm of the magnitude of the DFT of the EMF induced in search coil 1 in the end region.

TABLE II
INDUCED EMFS IN TWO SEARCH COILS AND TWO LOOPS

Current (A)		Simulations			Measurement
		Case 1	Case 2	Case 3	
500	$\tilde{\mathcal{E}}_{\mathrm{end}}$ (V)	0.31	0.35	0.34	0.36
	$\tilde{\mathcal{E}}_{\mathrm{act}}$ (V)	3.23	3.24	3.24	3.58
832	$\tilde{\mathcal{E}}_{\mathrm{end}}$ (V)	0.52	0.58	0.57	0.61
	$\tilde{\mathcal{E}}_{\mathrm{act}}$ (V)	5.38	5.40	5.40	5.61
1000	$\tilde{\mathcal{E}}_{\mathrm{end}}$ (V)	0.63	0.70	0.69	0.73
	$\tilde{\mathcal{E}}_{\mathrm{act}}$ (V)	6.47	6.49	6.50	6.86

are mainly 5th and 7th harmonics, but they are weak. The dc component in Fig. 7 probably comes from the offset of voltage in the oscilloscope.

C. Magnetic Flux

In the time-harmonic simulations, the phasor of the magnetic flux $\underline{\Phi}$ passing through the two loops was derived from

$$\underline{\Phi} = \oint_{\mathrm{C}} \underline{\boldsymbol{A}} \cdot \mathrm{d}\boldsymbol{l} \tag{7}$$

where C represents the integral path along the loops; and $\mathrm{d}\boldsymbol{l}$ is the vector differential of length. According to Faraday's law, the phasor of the induced EMF $\underline{\mathcal{E}}$ could be calculated by $\underline{\mathcal{E}} = -\mathrm{j}\omega\underline{\Phi}$, and then the rms value was $|\underline{\mathcal{E}}|/\sqrt{2}$.

The rms values of the induced EMFs in the measurement were given by the multimeters directly.

Table II lists the simulation results and measurements under three situations: $\tilde{I}_{\mathrm{ph}}^{\mathrm{str}} = 500$ A, 832 A, and 1000 A. Moreover, cases 1, 2, and 3 in Table II mean three different boundary conditions to model the end shield and frame, as explained in Section III-C. $\tilde{\mathcal{E}}_{\mathrm{end}}$ and $\tilde{\mathcal{E}}_{\mathrm{act}}$ in Table II correspond to the rms values of the EMFs induced in the two search coils or two loops. $\tilde{\mathcal{E}}_{\mathrm{act}}$ in the simulation results has been multiplied by 2 because the axial length of loop 2 was just half of that of search coil 2.

As for the induced EMF in search coil 1 or loop 1, $\tilde{\mathcal{E}}_{\mathrm{end}}$, the results in cases 2 and 3 in Table II are close to the measured values at all the three current values, in comparison with case 1. As a result, using a homogeneous Neumann boundary condition or an SIBC to model the end shield and frame gives more

TABLE III
INTEGRALS OF DIFFERENT COMPONENTS OF MAGNETIC INDUCTION ON SURFACES OF END SHIELD AND FRAME

		$I_r/I_{\rm ref}$	$I_\varphi/I_{\rm ref}$	$I_z/I_{\rm ref}$
Case 2	End shield	7%	8%	100%
	Frame	100%	6%	8%
Case 3	End shield	16%	22%	100%
	Frame	100%	15%	21%

accurate magnetic field in the end region than using a homogeneous Dirichlet boundary condition. It is reasonable because magnetic induction vectors should be approximately perpendicular or slightly oblique to the interface between the air and ferromagnetic materials, instead of being parallel to the interface.

A quantitative calculation was carried out to find the direction of the magnetic induction vectors on the surfaces of the end shield and frame. In the calculation, the absolute values of the real parts of the phasors of all the components, $|\mathrm{Re}\{\underline{B}_r\}|$, $|\mathrm{Re}\{\underline{B}_\varphi\}|$, and $|\mathrm{Re}\{\underline{B}_z\}|$, where Re means taking the real part of a complex number, were integrated on the end shield and frame, respectively. Further, the average values of the above integrals over one period were calculated as I_r, I_φ, and I_z, respectively. In both cases 2 and 3, on the surface of the end shield which was parallel to the $r-\varphi$ plane, I_z was chosen as a reference value $I_{\rm ref}$, and then the corresponding ratios $I_r/I_{\rm ref}$, $I_\varphi/I_{\rm ref}$, and $I_z/I_{\rm ref}$ were calculated, respectively. Similarly, on the surface of the frame which was parallel to the $\varphi-z$ plane, I_r was chosen as a reference value $I_{\rm ref}$, and then the same ratios were calculated. The results are listed in Table III. Obviously, in Table III, for both cases 2 and 3, axial magnetic induction is the main component on the surface of the end shield, and radial magnetic induction is the main component on the surface of the frame.

Besides, the difference between cases 2 and 3 is that no eddy current flows in the end shield and frame in case 2. However, these two cases give quite close results, so it is believed that the eddy current in the end shields and frame does not have distinct effects on the magnetic field in the end region.

On the other hand, in Table II, as for the induced EMF in search coil 2 or loop 2, $\tilde{\mathcal{E}}_{\rm act}$, the three cases at all the current values give quite close results. As a result, different boundary conditions used to model the end shields and frame of the machine do not have distinct effects on the magnetic field in the active region.

D. Magnetic Induction

In the measurement, magnetic induction was measured at two points, P1 and P2. P1 was in the end region, and P2 in the active region, as marked in Fig. 4. A Gauss/Tesla meter was used in the measurement, and the circular active area of the sensor of the probe was 2.48 mm^2. The rms values were given by the meter directly. In the time-harmonic simulations, the rms values of each component of magnetic induction were calculated at the same points. Table IV lists the results under the same cases as in Table II. $\tilde{B}_r$, $\tilde{B}_\varphi$, and $\tilde{B}_z$ denote the rms values of the radial, circumferential, and axial components of magnetic induction in the cylindrical coordinate system.

Some differences appear between the simulation results and measured values in $\tilde{B}_z$ at point P2 for all the cases. The reason comes from the fact that it was difficult to make the probe of the meter exactly perpendicular to the direction of the measured components. Because $\tilde{B}_z$ was quite small in the active region whereas $\tilde{B}_r$ and $\tilde{B}_\varphi$ were quite large, a slight deflection of the probe from the perpendicular position may introduce some components from $\tilde{B}_r$ and $\tilde{B}_\varphi$ into $\tilde{B}_z$.

Anyway, the simulation results and measurements are quite consistent except $\tilde{B}_z$ as explained above. As for point P1 at all the current values, cases 2 and 3 in the simulations give closer results to the measurements, and accordingly it is the same conclusion as drawn from Table II. It is also obvious that the axial component $\tilde{B}_z$ is not small in the end region by comparison with $\tilde{B}_r$ and $\tilde{B}_\varphi$, so the magnetic induction in the end region is definitely 3-D.

E. Induced EMF and Phase Voltage of Stator Winding

Current-driven as the numerical model was, the induced EMF of the phase winding should be approximately equal to the measured phase voltage in magnitude. There are six stator coils in a phase belt and therefore the phasor of the induced EMF of the phase winding $\underline{\mathcal{E}}_{\rm ph}$ was calculated by

$$\underline{\mathcal{E}}_{\rm ph} = -\mathrm{j}\omega \sum_{m=1}^{6} \underline{\Phi}_m \tag{8}$$

where $\underline{\Phi}_m$ is the phasor of the magnetic flux passing through a stator coil and was computed by (7). Because the slot leakage distributed unevenly along the radial height of a coil side, the middle line inside each coil was chosen as the integral path for calculating $\underline{\Phi}_m$.

The calculated rms value of the induced EMF by (8) was 162.5 V. The calculated resistive voltage drop in the stator winding was just 2.2 V, and it lead the induced EMF by 90°. Consequently, the calculated voltage was still 162.5 V. The measured rms value of the phase voltage was 168.4 V. That they are close validates the current-driven numerical model. Moreover, the magnetic slot wedges slightly affect the induced EMF of the phase winding. Without including the slot wedges, the induced EMF was 151.3 V.

VI. CONCLUSIONS

In this paper, the magnetic field in the end region of a 2.24-MW induction machine was studied by 3-D numerical simulations with different modeling conditions and then was compared with the measurements. In the simulations, to cope with the modeling of the end shields and frame, three familiar boundary conditions were used to replace these parts.

By comparison with the measurements, the use of a homogeneous Neumann boundary condition and a standard impedance boundary condition proves to be reasonable and gives more accurate results of the magnetic field in the end region than a homogeneous Dirichlet boundary condition. The eddy current in

TABLE IV
MAGNETIC INDUCTION AT TWO POINTS IN TEST MACHINE

Current (A)			Simulations			Measurement
			Case 1	Case 2	Case 3	
500	P1	$\tilde{B}_r$ (mT)	13.42	14.43	14.24	15.6
		$\tilde{B}_\varphi$ (mT)	15.66	16.24	16.11	17.6
		$\tilde{B}_z$ (mT)	17.26	16.75	16.86	18.6
	P2	$\tilde{B}_r$ (mT)	29.91	29.80	29.83	30.0
		$\tilde{B}_\varphi$ (mT)	28.12	28.15	28.14	28.3
		$\tilde{B}_z$ (mT)	1.46	1.34	1.38	5.2
832	P1	$\tilde{B}_r$ (mT)	22.36	24.05	23.71	25.6
		$\tilde{B}_\varphi$ (mT)	26.08	27.05	26.87	28.7
		$\tilde{B}_z$ (mT)	28.76	27.91	28.09	28.2
	P2	$\tilde{B}_r$ (mT)	49.82	49.64	49.68	49.4
		$\tilde{B}_\varphi$ (mT)	46.85	46.90	46.88	45.4
		$\tilde{B}_z$ (mT)	2.43	2.24	2.29	6.5
1000	P1	$\tilde{B}_r$ (mT)	26.88	28.92	28.51	28.3
		$\tilde{B}_\varphi$ (mT)	31.36	32.52	32.28	33.8
		$\tilde{B}_z$ (mT)	34.58	33.55	33.77	34.4
	P2	$\tilde{B}_r$ (mT)	59.91	59.68	59.73	61.4
		$\tilde{B}_\varphi$ (mT)	56.33	56.38	56.37	54.6
		$\tilde{B}_z$ (mT)	2.92	2.69	2.76	9.3

the end shields and frame does not affect the magnetic field evidently. In addition, by comparing the measured voltage and calculated voltage of the stator winding, the current-driven numerical model proves further to be effective and accurate. In conclusion, the consistency of the simulation results and measurements demonstrates that a current-driven time-harmonic numerical model with suitable boundary conditions can acquire a reliable analysis of the magnetic field in the end region.

The 3-D numerical model with a two-layer diamond winding is quite general and therefore the analysis method as well as the assignment of modeling conditions proposed in this paper can be used to analyze the magnetic field in the end region of other similar radial-flux electric machines. The model presented in this paper can also be applied to the calculation of the stator end-winding leakage reactance of a rotating electric machine.

ACKNOWLEDGMENT

This work was supported by the Finnish Foundation for Technology Promotion in Finland, and the Helsinki University of Technology in Finland. The authors thank the ABB Company in Finland for providing the test electric machine.

REFERENCES

[1] V. C. Silva, Y. Maréchal, and A. Foggia, "Surface impedance method applied to the prediction of eddy currents in hydrogenerator stator end regions," *IEEE Trans. Magn.*, vol. 31, no. 3, pp. 2072–2075, May 1995.

[2] V. C. Silva, G. Meunier, and A. Foggia, "A 3-D finite-element computation of eddy currents and losses in laminated iron cores allowing for electric and magnetic anisotropy," *IEEE Trans. Magn.*, vol. 31, no. 3, pp. 2139–2141, May 1995.

[3] Y. Yao, H. Xia, G. Ni, X. Liang, S. Yang, and P. Ni, "3-D eddy current analysis in the end region of a turbogenerator by using reduced magnetic vector potential," *IEEE Trans. Magn.*, vol. 42, no. 4, pp. 1323–1326, Apr. 2006.

[4] K. Yamazaki *et al.*, "Eddy current analysis considering lamination for stator core ends of turbine generators," *IEEE Trans. Magn.*, vol. 44, no. 6, pp. 1502–1505, Jun. 2008.

[5] G. K. M. Khan, G. W. Buckley, and N. Brooks, "Calculation of forces and stresses on generator end-windings—Part I: Forces," *IEEE Trans. Energy Conv.*, vol. 4, no. 4, pp. 661–670, Dec. 1989.

[6] K.-C. Kim, H.-W. Lee, Y.-D. Chun, and J. Lee, "Analysis of electromagnetic force distribution on end winding for motor reliance," *IEEE Trans. Magn.*, vol. 41, no. 10, pp. 4072–4074, Oct. 2005.

[7] Y. Liu and S. Hjärne, "Analysis of forces on coil ends of formed stator windings," in *Proc. Int. Conf. Electrical Machines and Systems*, Seoul, Korea, Oct. 2007, pp. 1019–1024.

[8] M. Ohtaguro, K. Yagiuchi, and H. Yamaguchi, "Mechanical behavior of stator endwindings," *IEEE Trans. Power App. Syst.*, vol. PAS-99, no. 3, pp. 1181–1185, May/Jun. 1980.

[9] R. Lin and A. Arkkio, "3-D finite element analysis of magnetic forces on stator end-windings of an induction machine," *IEEE Trans. Magn.*, vol. 44, no. 11, pp. 4045–4048, Nov. 2008.

[10] A. Merkhouf, B. F. Boueri, and H. Karmaker, "Generator end windings forces and natural frequency analysis," in *Proc. IEEE Int. Electric Machines and Drives Conference*, Madison, WI, Jun. 2003, vol. 1, pp. 111–114.

[11] M. R. Patel and J. M. Butler, "End-winding vibrations in large synchronous generators," *IEEE Trans. Power App. Syst.*, vol. PAS-102, no. 5, pp. 1371–1377, May 1983.

[12] C. Micallef, S. J. Pickering, K. A. Simmons, and K. J. Bradley, "Improved cooling in the end region of a strip-wound totally enclosed fan-cooled induction electric machine," *IEEE Trans. Ind. Electron.*, vol. 55, no. 10, pp. 3517–3524, Oct. 2008.

[13] J. Li, H. Li, and Z. Lu, "Research on temperature-rise of stator iron-core end region of turbine generator," in *Proc. 5th Int. Conf. Power Electronics and Drive Systems*, Singapore, Nov. 2003, vol. 1, pp. 766–770.

[14] G. K. M. Khan, G. W. Buckley, R. B. Bennett, and N. Brooks, "An integrated approach for the calculation of losses and temperatures in the end-region of large turbine generators," *IEEE Trans. Energy Conv.*, vol. 5, no. 1, pp. 183–194, Mar. 1990.

[15] R. Lin and A. Arkkio, "Calculation and analysis of stator end-winding leakage inductance of an induction machine," *IEEE Trans. Magn.*, vol. 45, no. 4, pp. 2009–2014, Apr. 2009.

[16] M.-F. Hsieh, Y.-C. Hsu, D. G. Dorrell, and K.-H. Hu, "Investigation on end winding inductance in motor stator windings," *IEEE Trans. Magn.*, vol. 43, no. 6, pp. 2513–2515, Jun. 2007.
[17] D. Ban, D. Žarko, and I. Mandić, "Turbogenerator end-winding leakage inductance calculation using a 3-D analytical approach based on the solution of Neumann integrals," *IEEE Trans. Energy Conv.*, vol. 20, no. 1, pp. 98–105, Mar. 2005.
[18] R. De Weerdt, E. Tuinman, K. Hameyer, and R. Belmans, "Finite element analysis of steady state behavior of squirrel cage induction motors compared with measurements," *IEEE Trans. Magn.*, vol. 33, no. 2, pp. 2093–2096, Mar. 1997.
[19] Y. Guo, J. Zhu, J. Zhong, H. Lu, and J. Jin, "Measurement and modeling of rotational core losses of soft magnetic materials used in electrical machines: A review," *IEEE Trans. Magn.*, vol. 44, no. 2, pp. 279–291, Feb. 2008.
[20] A. Schramm and D. Gerling, "Analytical calculation of the end winding leakage inductance based on the solution of Neumann integrals," in *Proc. IEEE Int. Symp. Industrial Electronics*, Dubrovnik, Croatia, Jun. 2005, vol. 2, pp. 851–855.
[21] B. Frei-Spreiter and K. Reichert, "Calculation of end winding fields of turbogenerators by integral methods for modelling mechanical characteristics," *IEEE Trans. Magn.*, vol. 34, no. 5, pp. 3636–3639, Sep. 1998.
[22] E. Plantive, S. Salon, M. V. K. Chari, and N. Richard, "Advances in the axiperiodic magnetostatic analysis of generator end regions," *IEEE Trans. Magn.*, vol. 32, no. 5, pp. 4278–4280, Sep. 1996.
[23] J. Weiss and C. M. Stephens, "Finite elements for three-dimensional magnetostatic fields and its application to turbine-generator end regions," *IEEE Trans. Power App. Syst.*, vol. PAS-100, no. 4, pp. 1591–1596, Apr. 1981.
[24] Y. Liang and W. Chen, "Numerical calculation of stator end-leakage reactance of large turbogenerator," in *Proc. 5th Int. Conf. Electrical Machines and Systems*, Shenyang, China, Aug. 2001, vol. 1, pp. 170–173.
[25] R. De Weerdt and R. Belmans, "Squirrel cage induction motor end effects using 2D and 3D finite elements," in *Proc. 7th Int. Conf. Electrical Machines and Drives*, Durham, U.K., Sep. 1995, no. 412, pp. 62–66.
[26] W.-R. Novender and W. Müller, "3-dimensional nonlinear calculations of magnetic fields in turbogenerators," *IEEE Trans. Magn.*, vol. MAG-19, no. 6, pp. 2604–2607, Nov. 1983.
[27] J. Li, Y. Sun, and G. Yang, "Calculation and analysis of 3D magnetic field for end region of large turbogenerators," in *Proc. 8th Int. Conf. Electrical Machines and Systems*, Nanjing, China, Sep. 2005, vol. 3, pp. 2079–2082.
[28] V. C. Silva, G. Meunier, and A. Foggia, "A 3-D finite-element computation of eddy currents and losses in the stator end laminations of large synchronous machines," *IEEE Trans. Magn.*, vol. 32, no. 3, pp. 1569–1572, May 1996.
[29] S. Richard, J.-P. Ducreux, and A. Foggia, "A three dimensional finite element analysis of the magnetic field in the end region of a synchronous generator," in *Proc. IEEE Int. Electric Machines and Drives Conf.*, Milwaukee, WI, May 1997, pp. WC2/4.1–WC2/4.3.
[30] C. Sadarangani, *Electrical Machines-Design and Analysis of Induction and Permanent Magnet Motors*. Stockholm, Sweden: KTH Royal Inst. Technol., 2000, p. 126.

Ranran Lin was born in Beijing, China, in 1980. He received the B.Sc. degree in engineering from Shanghai Jiao Tong University, Shanghai, China, in 2002, and the M.Sc. degree in technology from Helsinki University of Technology, Espoo, Finland, in 2004.

He is a Research Scientist with the Department of Electrical Engineering, Faculty of Electronics, Communications and Automation, Helsinki University of Technology. His current research interests include the numerical analysis of electromagnetic field and mechanical vibrations in the end region of large rotating electric machines.

Mr. Lin was a Session Chair of 2008 IEEE International Magnetics Conference held in Madrid, Spain.

Ari Haavisto was born in Huittinen, Finland, in 1968. He received the B.Sc. degree in electrical engineering from Satakunta University of Applied Sciences, Pori, Finland, in 1994, and the M.Sc. degree in technology from the Helsinki University of Technology, Espoo, Finland, in 2006.

At present, he is an Operations Engineer with the Department of Electrical Engineering, Faculty of Electronics, Communications and Automation, Helsinki University of Technology. His current research interests include the thermal modelling of electric machines.

Antero Arkkio was born in Vehkalahti, Finland, in 1955. He received the M.Sc. degree in technology and the D.Sc. degree in technology from the Helsinki University of Technology, Espoo, Finland, in 1980 and 1988, respectively.

He has been working with various research projects, which deal with the modeling, design, and measurement of electric machines. He is a Professor of electrical engineering at the Helsinki University of Technology. He was a Senior Research Scientist and then a Laboratory Manager at the same university.